Journal of Advanced Ceramics
2024, **13**(10): 1655–1665
https://doi.org/10.26599/JAC.2024.9220967

Research Article

Power capacity enhancement and loss reduction induced by limited solid solubility of Ho^{3+} rare-earth substitution in NiCuZn spinel ferrites

Hanyu Zhang, Qifan Li, Xiaona Jiang, Chuanjian Wu, Ke Sun, Zhongwen Lan, Zhong Yu✉

School of Materials and Energy, University of Electronic Science and Technology of China, Chengdu 610054, China

Received: July 4, 2024; Revised: August 20, 2024; Accepted: September 7, 2024

Abstract: The application of NiCuZn ferrites (NCZFs) in high-power communication systems is constrained by their nonlinear excitation. To reduce nonlinear effects, it is essential for ferrite materials to possess a relatively high spin-wave linewidth (ΔH_k). Doping with ions such as cobalt and rare-earth (RE) ions with fast relaxation has proven effective in increasing ΔH_k of ferrites. However, the regulatory mechanism of doping NCZFs with RE ions with larger ionic radii remains unclear. In this study, Ho^{3+}-substituted NCZFs were synthesized via a solid-state reaction route. The spatial distribution and substitution amount of the Ho^{3+} ions were carefully investigated via elemental and phase composition analysis, revealing the limited solid solubility of the Ho^{3+} ions in NCZFs. Some of the Ho^{3+} ions enter the lattice and occupy the octahedral sites, accelerating relaxation and increasing ΔH_k to a maximum value of 2.63 kA·m^{-1}. Insoluble Ho^{3+} ions combine with Fe^{3+} ions to form a $HoFeO_3$ heterogeneous phase with Fe^{3+} ions at the grain boundaries, leading to iron deficiency within NCZF crystals and significantly reducing the dielectric loss tangent at microwave frequencies. These results reveal the great potential of Ho^{3+}-substituted NCZFs for high-power, low-loss microwave applications.

Keywords: NiCuZn ferrites (NCZFs); rare earth; solid solubility; spin-wave linewidth; dielectric loss

1 Introduction

NiCuZn ferrites (NCZFs) are extensively utilized as the core material in microwave circulators for high-frequency (X–Ka band) communication systems because of their high saturation magnetization ($4\pi M_s$, up to 400 kA·m^{-1}), resistivity ($\rho > 1$ MΩ·m), and exceptional gyromagnetic properties [1–3]. As one of the most significant components in microwave communication systems, circulators are extensively applied in satellite communication, phased array radar, and electronic countermeasures. They play crucial roles in isolating high-power signals, protecting circuit systems, segregating signals, and reducing interference due to their unidirectional transmission characteristics. The free space path loss of a signal is proportional to the square of the product of the transmission distance and the carrier frequency (f). As communication technology progresses toward higher frequencies and longer distances, signal attenuation during transmission inevitably worsens [4,5]. Enhancing the power of the signal source is an effective method to counteract the attenuation of high-frequency signals during transmission. However, high-power electromagnetic pulses (EMPs) with intense microwave fields (h) can excite nonlinear effects in microwave ferrite devices, potentially leading to device failure [6,7].

The maximum carrying power (P_{max}) of a microwave ferrite device is proportional to the square of the threshold magnetic field (h_c) of the ferrite material. To counter the threat posed by high-power EMPs to communication systems, enhancing h_c is an effective solution. The relationship between h_c and the material properties can be expressed as Eq. (1):

$$h_c = \frac{f \cdot \Delta H_k}{\gamma \cdot 4\pi M_s} \tag{1}$$

where ΔH_k and γ represent the spin-wave linewidth and gyromagnetic ratio, respectively. Therefore, microwave ferrites with a high ΔH_k are crucial to ensure that circulators have sufficient power-carrying capacity [8,9]. Long *et al.* [10] measured the critical distortion of the output waveforms of different gyromagnetic ferrites via a microwave pulse signal source with adjustable f and h values to determine ΔH_k values of the samples. The results revealed a positive correlation between ΔH_k and P_{max}, and the sample with a ΔH_k of 1.91 kA·m^{-1} achieved a P_{max} of up to 66.7 kW. Cui *et al.* [11] assembled NiZn ferrite cores with different gyromagnetic parameters into a gyromagnetic nonlinear transmission line, which typically operates at 10–1000 MW, and investigated the impact of these parameters on the output microwave signal. They reported that P_{max} could reach 155 MW at a ΔH_k of 3.57 kA·m^{-1}. Vehkalahti [12] compared two different ferrite materials and reported that a circulator made with a higher ΔH_k material has a stronger power handling capability, rated at 35 kW, which is 3.5 times the average power requirement. Additionally, NCZFs should possess a narrow ferromagnetic resonance linewidth (ΔH) and low microwave dielectric loss ($\tan\delta_\varepsilon$), which are beneficial for minimizing the forward transmission loss of the signal in circulators [13,14].

The grain size miniaturization and doping of fast-relaxing ions are effective strategies for increasing the ΔH_k of polycrystalline

✉ Corresponding author.
E-mail: yuzhong@uestc.edu.cn

ferrites [15–18], whereas the appropriate cation species, ion occupancy, and densification are crucial for optimizing ΔH and $\tan\delta_\varepsilon$ [19–23]. These considerations necessitate careful microstructure and formulation design. From a microstructural perspective, lowering the sintering temperature during the solid-phase reaction can effectively decrease the grain size. However, this may result in insufficient densification of polycrystalline ferrite, leading to increased pores and consequently exacerbating ΔH and $\tan\delta_\varepsilon$. Therefore, some researchers [9] have utilized the uniaxial hot-pressing technique to ensure the densification of sintered samples with limited grain sizes. Although this method successfully reduces ΔH and maintains ΔH_k at a certain level, the limited grain uniformity and complexity of the process hinder its large-scale applicability. Additionally, the combination of appropriate flux agents (e.g., Bi_2O_3, V_2O_5, and glass) [24–27] and crystallization inhibitors (e.g., $BaTiO_3$, Al_2O_3, ZrO_2, and other high melting point substances) [28–30] as additives can effectively regulate the grain growth process, leading to the attainment of a compact microstructure with uniform grains, thereby optimizing the microwave characteristics.

As spinel-structured ferrites, there are two types of crystallographic cation sites in the unit cell of NCZFs, i.e., 8 fourfold tetrahedral (A) sites and 16 sixfold octahedral (B) sites [2]. In recent decades, extensive research has been conducted on improving the microwave properties of NCZFs via cation substitution. The substitution of nonmagnetic ions, which lack magnetic crystalline anisotropy, for some magnetic ions can effectively diminish the absolute value of the crystalline anisotropy constant ($|K_1|$). This substitution helps mitigate the negative impact of the crystalline anisotropy-induced linewidth (ΔH_a) on ΔH [21,31,32]. The iron-deficient formulations can efficiently suppress Fe^{2+} generation, consequently reducing the possibility of electron transitions between Fe^{2+} and Fe^{3+} and reducing $\tan\delta_\varepsilon$ [23]. The strong spin-orbit coupling of Co^{2+} and RE ions enables rapid energy transfer from spin waves to the lattice, thus shortening the relaxation time (τ_k). These ions are referred to as fast-relaxing ions. In the field of microwave gyromagnetic ferrites, researchers typically employ Co^{2+} ions, which have smaller ionic radii, to adjust the ΔH_k of spinel ferrites [33–36], whereas RE ions are utilized for yttrium iron garnet (YIG) microwave ferrites because of their larger lattice spaces [8,17]. Unlike Co^{2+}, which is a 3d magnetic ion, 4f shell layer of RE ions is embedded within the $5s^25p^6$ full-electron shell layer. Consequently, 4f electrons of RE ions have a larger effective solid charge and experience a stronger central field than 3d electrons of Co^{2+}, which results in the average radius of the 4f shell layer being approximately half that of the 3d shell layer of Co^{2+}. Since spin–orbit coupling is inversely proportional to the cube of the electron orbital radius, RE ions exhibit stronger spin-orbit coupling, which effectively enhances the power-carrying capacity of microwave ferrites. Furthermore, the substitution of fast-relaxing ions inevitably increases the contribution of ΔH_a to ΔH, which contradicts the requirement for a narrow ΔH and high ΔH_k. Therefore, it is crucial to precisely control the substitution amount to avoid excessive insertion loss in circulators.

Schlömann *et al.* [37] summarized the impact of various RE ions, including Ho^{3+}, Dy^{3+}, and Sm^{3+}, on the microwave power characteristics of YIG and reported that Ho^{3+} has a superior gain effect and that each substitution of 0.1 increases ΔH_k by 4.80 kA·m^{-1}. Additionally, Ho^{3+} has a high ionic magnetic moment (10.61 μB, μB is the Bohr magneton, indicating the smallest unit of the orbital magnetic moment) and a relatively small ionic radius (0.901 Å) [38], making it an excellent candidate for substitution in spinel ferrites. To further elucidate the mechanism of Ho^{3+} in NCZFs, Ho^{3+}-substituted NCZFs with a composition of $Ni_{0.505}Cu_{0.1}Zn_{0.4}Co_{0.015}Fe_{1.98-x}Ho_xO_4$ (x = 0.00–0.04) were prepared via a solid-state reaction method and comprehensively investigated in this study. Remarkably, the restricted solid solubility of Ho^{3+} in NCZFs results in the predominant phase remaining iron deficient and an optimized microstructure. ΔH_k increases while $\tan\delta_\varepsilon$ decreases. The separation of ΔH revealed that the optimization of the microstructure partially mitigated the negative effect of the increased $|K_1|$. The results provide an important basis and guidance for the development of high-power, low-loss microwave gyromagnetic ferrites by substituting spinel ferrite with RE ions.

2 Experimental

2.1 Specimen fabrication

NCZF samples with a composition of $Ni_{0.505}Cu_{0.1}Zn_{0.4}Co_{0.015}Fe_{1.98-x}Ho_xO_4$ (x = 0.00–0.04) were prepared via a solid-state reaction method. First, highly purified powders of NiO (98.1%), ZnO (99.7%), CuO (99%), Co_2O_3 (99%), Fe_2O_3 (99.3%), and Ho_2O_3 (99.99%) with deionized water were milled into a slurry in a planetary mill (QM-3SP4, Chishun Tech, China) for 3 h, and the slurry was transferred into an oven (KW-101, Kewei, China) to dry at 80 °C. Second, the samples were calcined at 900 °C for 3 h. Then, 0.15 wt% Bi_2O_3, 0.12 wt% CaO, and 0.10 wt% $BaTiO_3$ were added to the powders as additives, and the powders were milled into a slurry again for 6 h. Afterward, the slurry was dried again and granulated with 12 wt% polyvinyl alcohol (PVA). Eventually, NCZF particles were separately pressed into discs (12 mm in diameter) and sintered at 1030–1070 °C for 3 h for densification.

2.2 Material characterization

Bulk density (D_{bulk}) was obtained using the Archimedes method. The theoretical density of polycrystalline ferrite (D_{PF}) is calculated as Eq. (2):

$$D_{PF} = \frac{D_{xrd\text{-}NCZF} + D_{xrd\text{-}HFO} \cdot wt\%_{HFO}}{1 + wt\%_{HFO}} \quad (2)$$

where $D_{xrd\text{-}NCZF}$ and $D_{xrd\text{-}HFO}$ are X-ray densities of NCZFs and $HoFeO_3$, respectively, and the weight percentage of $HoFeO_3$ ($wt\%_{HFO}$) represents the weight percentage of $HoFeO_3$ corresponding to one NCZF. In the case of polycrystalline ferrites, porosity (P) can be derived from D_{bulk} and D_{PF} via Eq. (3):

$$P = \frac{D_{bulk} - D_{PF}}{D_{bulk}} \times 100\% \quad (3)$$

The crystal structure was determined via an X-ray diffractometer (XRD; Aeris Benchtop, PANalytical, the Netherlands) with Cu Kα radiation over a 2θ range from 20° to 80° at steps of 0.02°. The microstructures were observed via a backscattered electron (BSE; Phenom Pharos, Thermo Scientific, USA) scanning microscope, and the element composition and distributions were characterized via an energy dispersive spectrometer (EDS; Phenom Pharos, Thermo Scientific, USA). The magnetic hysteresis loops were measured by a vibrating sample magnetometer (VSM; Lake Shore 8604, Lake Shore, USA) with a maximum magnetic field of 796 kA·m^{-1} at room temperature. ΔH of spherical samples (diameter of approximately 0.8 mm) was measured via TE_{106} perturbation cavity resonator via a vector network analyzer (Agilent N5227A, Agilent, USA) at ~9.3 GHz. ΔH_k was measured via the spin-wave linewidth test

system (эм6-27, Southwest Institute of Applied Magnetism, China). Cole–cole plots were measured by an impedance analyzer (E4991B, Keysight, USA) at frequencies of 1 MHz–1 GHz at room temperature. ρ values of samples were measured with a insulation resistance meter (TH2683A, Tonghui, China). Dielectric constant (ε') and tanδ_ε were measured by a cylindrical TM_{010} resonant cavity (DH406B, Dahua Electronic, China) at ~9.3 GHz.

3 Results and discussion

3.1 Crystal structure and phase composition

Figure 1 shows XRD patterns of Ho^{3+}-substituted NCZFs. All the diffraction pattern samples confirmed that the main crystalline phase was the spinel structure (PDF#08-0234), with a space group of *Fd*3*m* [36,39]. For the samples with x = 0.01–0.04, the second phase of the orthorhombic perovskite structure ($HoFeO_3$, PDF#74-1479) with a space group of *Pbnm* [36,40] is observed. The characteristic peaks of $HoFeO_3$ gradually become evident with increasing x, as shown in Fig. 1(f). The reason for this phenomenon is that the radius of the Ho^{3+} ions (0.901 Å) is larger than that of the Fe^{3+} ions (0.645 Å) [38], which restricts their accommodation in the B sites of the spinel lattice. Consequently, the unaccommodated Ho^{3+} ions diffuse to the grain boundaries and combine with Fe^{3+} ions from the spinel lattice, forming the second phase $HoFeO_3$, as evidenced by the subsequent EDS mapping and spot scanning results. This observation aligns with results reported by various authors [21,36,41].

To further verify and determine the crystal structure, ion occupancy, and crystalline phase ratio of NCZFs, XRD patterns were refined via Rietveld refinement via GSAS-II software version 4776 [42], and the results are presented in Tables 1 and 2. Rietveld refined XRD patterns were related to reliability factors. Namely, weighted profile coefficient (R_{wp}) and goodness factor (χ^2), are given in Fig. 1, and all of them are within reliable limits. Table 1 lists the cation distributions extracted from the Rietveld refinement of the measured XRD patterns: Zn^{2+} and Fe^{3+} ions predominantly occupy A sites, whereas Ni^{2+}, Cu^{2+}, Co^{2+}, Ho^{3+}, Fe^{3+}, and very small amounts of Zn^{2+} ions occupy B sites. The reason for this is that the height of the potential barrier that determines the difficulty of moving ions

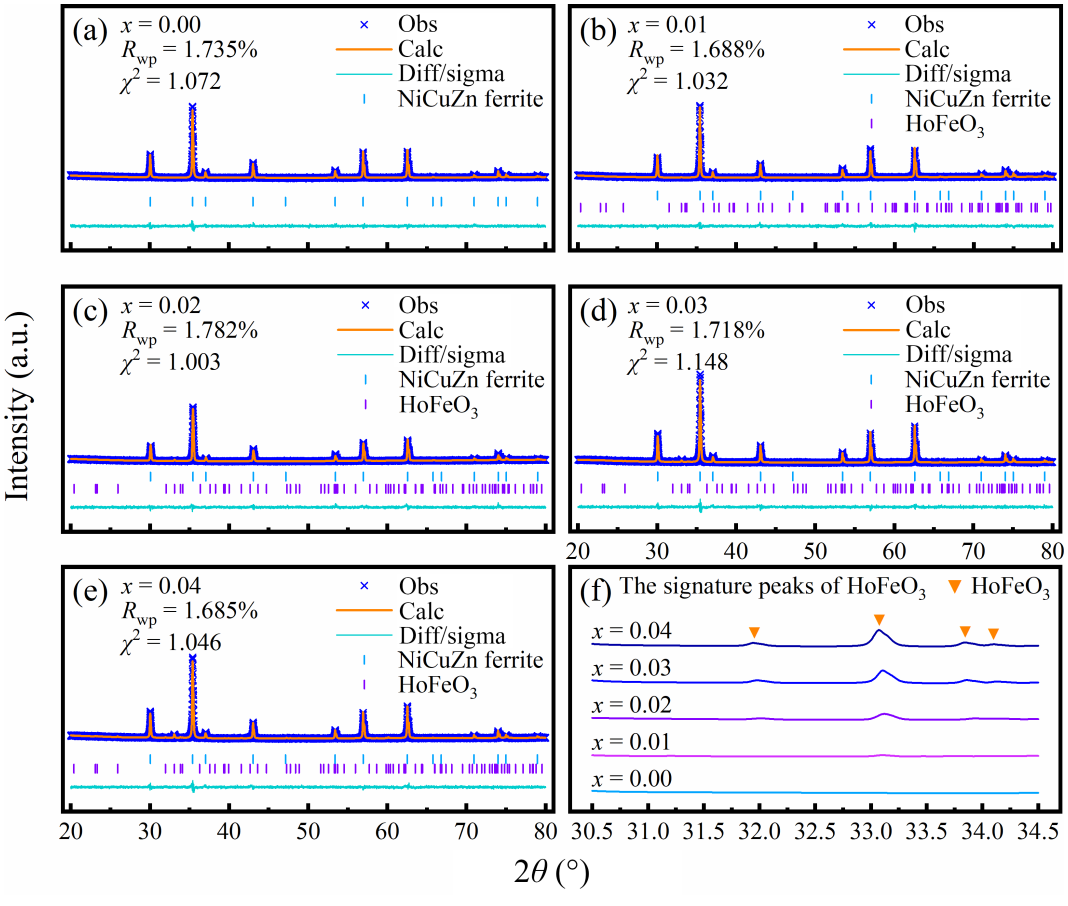

Fig. 1 XRD patterns and Rietveld-refined profiles of $Ni_{0.505}Cu_{0.1}Zn_{0.4}Co_{0.015}Fe_{1.98-x}Ho_xO_4$ spinel ferrite samples sintered at 1030 °C: (a) x = 0.00, (b) x = 0.01, (c) x = 0.02, (d) x = 0.03, (e) x = 0.04, and (f) signature peaks of $HoFeO_3$.

Table 1 Occupancy distribution of cations on A and B lattice sites of $Ni_{0.505}Cu_{0.1}Zn_{0.4}Co_{0.015}Fe_{1.98-x}Ho_xO_4$ ferrites extracted via Rietveld refinement

x	A site	B site
0.00	$(Zn_{0.3886}Fe_{0.6114})$	$[Ni_{0.2525}Cu_{0.05}Zn_{0.0057}Co_{0.0075}Ho_{0.0000}Fe_{0.6843}]$
0.01	$(Zn_{0.3842}Fe_{0.6104})$	$[Ni_{0.2525}Cu_{0.05}Zn_{0.0079}Co_{0.0075}Ho_{0.0012}Fe_{0.6760}]$
0.02	$(Zn_{0.3789}Fe_{0.6078})$	$[Ni_{0.2525}Cu_{0.05}Zn_{0.0106}Co_{0.0075}Ho_{0.0024}Fe_{0.6685}]$
0.03	$(Zn_{0.3677}Fe_{0.6044})$	$[Ni_{0.2525}Cu_{0.05}Zn_{0.0161}Co_{0.0075}Ho_{0.0032}Fe_{0.6615}]$
0.04	$(Zn_{0.3588}Fe_{0.5967})$	$[Ni_{0.2525}Cu_{0.05}Zn_{0.0206}Co_{0.0075}Ho_{0.0042}Fe_{0.6558}]$

such as Ni^{2+}, Cu^{2+}, Co^{2+}, and Ho^{3+} to the A-site is significantly greater than that of Zn^{2+} [43]. Fe^{3+} ions occupy the A and B sites at an ionic ratio of ~1:2, which is consistent with previous reports [44]. As the amount of Ho^{3+} substitution increases, the total number of cations on the A and B sites decreases, indicating an increase in the number of vacancies on this sublattice.

The solid solution limit of ions at lattice sites is determined by the oxidation state and ionic radius. Ho^{3+} ions clearly exhibit limited solid solubility in the octahedral sublattice of spinel ferrite because of their relatively large ionic radius. As depicted in Fig. 1(b), when x = 0.01, the sintered body contains a heterophase of $HoFeO_3$, with an increasing content of $HoFeO_3$ observed as x increases. The content of Ho^{3+} ions in NCZF does not remain constant with increasing substitution amount. Instead, it continues to increase while maintaining a ratio of approximately 5:1 between the substitution amount and the content of Ho^{3+}. This phenomenon can be attributed to excess Ho^{3+} ions combining with Fe^{3+} ions within the main lattice, forming another phase, $HoFeO_3$, which competes for additional capacity space for incorporating Ho^{3+} ions into the main lattice.

Lattice constant (a) of NCZFs $D_{xrd\text{-}NCZF}$, $D_{xrd\text{-}HFO}$, and $wt\%_{HFO}$ were obtained by refining XRD peaks of polycrystalline ferrites. D_{PF} and P of polycrystalline ferrites can be calculated from the above data as well as Eqs. (2) and (3). All the above parameters of polycrystalline ferrites are listed in Table 2. For the sample with Ho^{3+} substitution, the refinement results revealed the existence of a small amount of $HoFeO_3$ phase with a perovskite structure mixed with the spinel phase, whereas the samples without Ho^{3+} substitution exhibited a pure-phase composition. $HoFeO_3$ is antiferromagnetic and weakly ferrimagnetic in an external magnetic field at room temperature [40]. According to the refinement results, the weight percentage of $HoFeO_3$ in the samples increased from 0.4 to 1.8 wt% as x increased, which is expected to have a negligible effect on the magnetic properties of the samples.

As x increased, the lattice constant of NCZF initially tended to increase but then decreased, which indicated that Ho^{3+} ions with larger ionic radii could replace Fe^{3+} ions in the lattice to occupy the B sites, leading to lattice expansion. However, owing to the limited holding capacity of B sites for Ho^{3+} ions, those unable to enter the lattice combine with Fe^{3+} ions in NCZFs, resulting in the formation of $HoFeO_3$. As indicated in Table 1, the substitution of Ho^{3+} ions leads to cation deletion at both the A and B sites, leading to an increase in the number of vacancies on the sublattice and causing lattice collapse [23]. The variation in the lattice constant values is a consequence of Ho^{3+} ions entering the lattice in collaboration with the vacancies on the sublattice.

3.2 Microstructure and elemental distribution

Figure 2 shows BSE microscopy images, average grain size (D) distribution analysis, and P of NCZFs. BSE images were taken from the natural cross-section of the sintered body sintered at 1030 °C. The images were statistically analyzed for grain size distribution via ImageJ software (version 1.54d) [45] with the linear intercept method, revealing a normal distribution in all the cases. The grain size distribution curves exhibited narrower peak shapes, and the standard deviation of the grain size distribution decreased with increasing Ho^{3+} substitution, as shown in Fig. 2(f). This suggests that the substitution of Ho^{3+} ions results in a more homogeneous microstructure of the sintered sample and an optimized microstructure of NCZFs.

The impact of ionic substitution on sintering characteristics is profound [24,46] and can promote or inhibit the grain growth and densification process of polycrystalline ferrite during sintering to a certain extent. Since the binding energy of Ho^{3+}–O^{2-} bond is greater than that of Fe^{3+}–O^{2-} bond, the introduction of Ho^{3+} alters the kinetic process of the solid-state reaction and hinders the reaction [47]. Additionally, the heterogeneous phase $HoFeO_3$ generated during the substitution process is pinned at the grain boundaries, which inhibits the diffusion and migration of the grain boundaries and impedes grain growth, contributing to the establishment of a more homogeneous microstructure [22,28,29]. Consequently, the grains of polycrystalline ferrites were miniaturized with increasing x at each sintering temperature, as shown in Fig. 2(g). P is an essential parameter for characterizing the degree of densification in sintered bodies. Obviously, the introduction of Ho^{3+} alleviates the abnormal grain growth in polycrystalline ferrite and promotes the evacuation of pores. However, excessive substitution weakens the densification during sintering, polycrystalline ferrites are insufficiently densified, and the pores are incompletely evacuated. Consequently, P has a minimum value when x increases, as shown in Fig. 2(h).

Furthermore, an increase in sintering temperature can promote the generation of a liquid phase and the mass transfer of ions, thereby driving the occurrence of grain boundary diffusion and migration during the sintering process [48,49]. Excessively low sintering temperatures cause insufficient densification of sintered bodies, many unclosed pores at the grain boundaries, and loose grain arrangements. Appropriate sintering temperatures result in the formation of liquid phases that uniformly fill the pores and promote ionic mass transfer for grain boundary diffusion, resulting in optimal densification of the sintered bodies and minimization of P. However, excessively high sintering temperatures can cause rapid diffusion at grain boundaries and even ion volatilization, leading to premature closure of pores that cannot be filled, subsequently deteriorating the microstructure, resulting in abnormal grain growth, and ultimately increasing P [25]. Accordingly, D is positively correlated with the sintering temperature, and the position of the lowest P value also increases as the sintering temperature increases.

The elemental distribution in NCZFs was investigated via EDS mapping and spot scanning, as shown in Fig. 3. Fe^{3+}, Zn^{2+}, and Co^{2+} ions were uniformly distributed in NCZF sintered bodies. Trace amounts of Ni and Cu are enriched. During the

Table 2 a, $D_{xrd\text{-}NCZF}$, $D_{xrd\text{-}HFO}$, $wt\%_{HFO}$, D_{PF}, and P

x	NCZF		$HoFeO_3$		Polycrystalline ferrite	
	a (Å)	$D_{xrd\text{-}NCZF}$ (g·cm^{-3})	$D_{xrd\text{-}HFO}$ (g·cm^{-3})	$wt\%_{HFO}$	D_{PF} (g·cm^{-3})	P (%)
0.00	8.38578	5.353	—	—	5.353	0.88
0.01	8.38871	5.345	7.851	0.4	5.355	0.51
0.02	8.38638	5.355	7.950	0.9	5.378	0.62
0.03	8.38562	5.374	7.954	1.3	5.408	0.71
0.04	8.38671	5.385	7.957	1.8	5.431	0.69

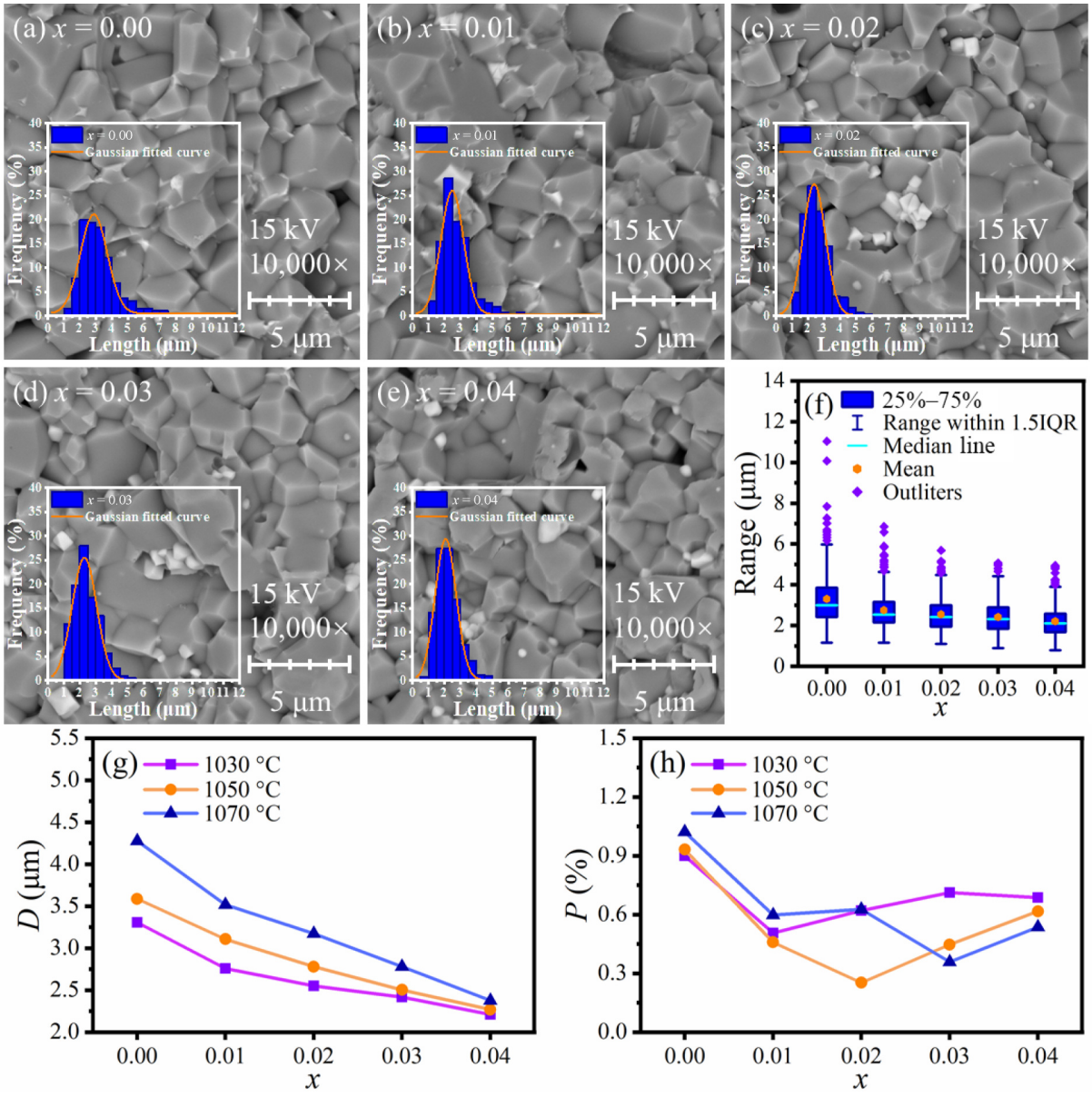

Fig. 2 BSE images and grain size distributions of $Ni_{0.505}Cu_{0.1}Zn_{0.4}Co_{0.015}Fe_{1.98-x}Ho_xO_4$ ferrite samples sintered at 1030 °C: (a) $x = 0.00$, (b) $x = 0.01$, (c) $x = 0.02$, (d) $x = 0.03$, and (e) $x = 0.04$. (f) Statistical analysis of grains. (g) D and (h) P of $Ni_{0.505}Cu_{0.1}Zn_{0.4}Co_{0.015}Fe_{1.98-x}Ho_xO_4$ ferrite samples sintered at different temperatures.

densification and grain growth stages of the sintering process of NCZFs, nickel and copper oxides precipitate, which is caused by the oxygen-deficient environment during the solid-phase reaction process [50,51]. This issue can be addressed by prolonging the holding time or introducing an oxygen atmosphere during the sintering process. In addition, Ho^{3+} substitution resulted in iron deficiency in NCZFs, which exacerbated the segregation of the ZnO phase [52], and the volatilization of Zn^{2+} [53] during sintering resulted in the enrichment of Ni and Cu. The segregation of the ZnO phase also inhibited the crystallization and growth of spinel ferrite to a certain extent, which contributed to the miniaturization of NCZF grains. Bi^{3+} ions (1.03 Å) [38] with a large ionic radius were added into NCZF as fluxes and enriched at the grain boundaries between grains. With increasing x, bright spots representing elemental Ho gradually appeared in the image, and the number of bright spots gradually increased, indicating that the solid solubility of RE ion Ho^{3+} in NCZF was limited.

In BSE microscopy, when the incident electron beam strikes the surface of the observed sample, the escaping electrons undergo elastic and inelastic collisions in irregular directions. The number of emitted electrons is influenced by the angle of incidence and the atomic number of the substance [54,55]. The number of scattered incident electrons is proportional to the atomic number, and elements with a higher atomic number have greater brightness in the image. EDS spot scanning and elemental content analysis were performed on the bright spot regions and gray regions in the image, respectively, and the results are shown in Fig. 3. When $x = 0.00$, the bright spot regions in the image exist at the grain boundary of NCZF, and the main component is Bi_2O_3 as flux. When $x = 0.04$, bright spots exist outside the NCZF grains in the form of crystalline grains. Analyses revealed that the primary composition of these bright spots was $HoFeO_3$ crystals, confirming that part of Ho^{3+}, which is unable to enter NCZF lattice, combines with Fe^{3+} to form the $HoFeO_3$ subcrystalline phase. EDS point-scan analysis results of the darker regions in the image are consistent with XRD refinement results.

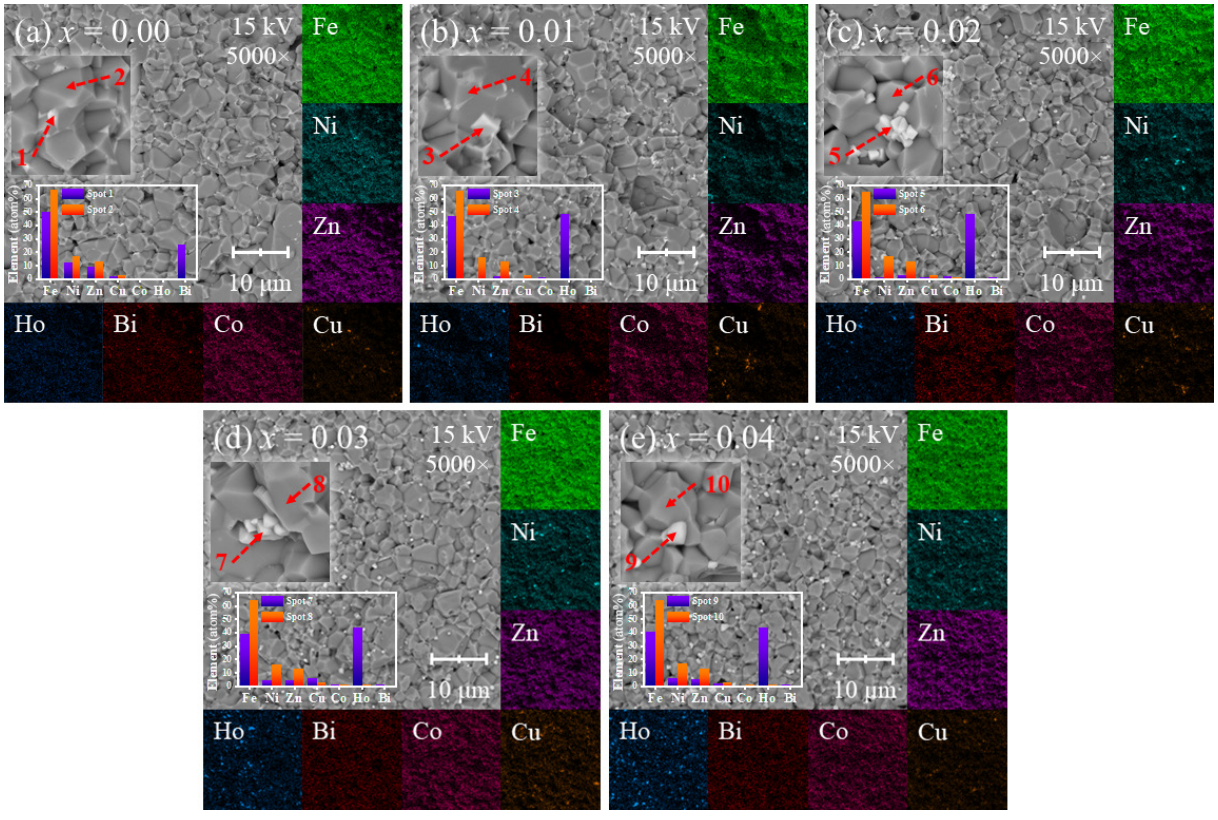

Fig. 3 Elemental distribution of $Ni_{0.505}Cu_{0.1}Zn_{0.4}Co_{0.015}Fe_{1.98-x}Ho_xO_4$ ferrite samples sintered at 1030 °C, as investigated via EDS mapping and spot scanning: (a) $x = 0.00$, (b) $x = 0.01$, (c) $x = 0.02$, (d) $x = 0.03$, and (e) $x = 0.04$.

3.3 Magnetic properties

$4\pi M_s$ was obtained by measuring a series of hysteresis loops of the Ho^{3+}-substituted NCZF samples with different sintering temperatures at room temperature, as shown in Fig. 4(a). $4\pi M_s$ monotonically decreases with increasing Ho^{3+} substitution. The cations in spinel ferrite occupy two crystallographically distinct interstitial sites, A and B sites. The strong superexchange interactions between the cations in the 8a and 16d sites result in an antiparallel arrangement of magnetic moments in these sublattices. Consequently, the molecular magnetic moment is the difference between the magnetic moments of the tetrahedral and octahedral sublattices [56]. In Ho^{3+}-substituted spinel ferrites, although Ho^{3+} ions, with larger ionic magnetic moments, prefer to occupy B sites and replace Fe^{3+} ions, their solid solubility in NCZFs is limited. Instead, they combine with Fe^{3+} ions in the main crystalline phase to form the heterogeneous phase of $HoFeO_3$, inducing iron deficiency in the main crystalline phase. This results in a decrease in the molecular magnetic moment in the ferrite, leading to a gradual reduction in the number of $4\pi M_s$.

D and P are two significant factors influencing the $4\pi M_s$ of sintered bodies. As shown in Fig. 2, an increase in sintering temperature leads to a larger D, changes in P, and, consequently, fluctuations in $4\pi M_s$ [20]. Larger grains in polycrystalline ferrites indicate more complete crystallization, resulting in fewer grain boundaries and defects. This facilitates the movement of magnetic domain walls, thereby enhancing the number of $4\pi M_s$. However, excessively large grains may introduce defects such as pores, which can adversely affect the number of $4\pi M_s$. Therefore, it is crucial to control D within an optimal range. Additionally, the presence of pores reduces the effective volume of the magnetic material, decreasing the number of magnetic ions participating in the magnetization process. As nonmagnetic regions, pores disrupt the arrangement of magnetic domain structures and hinder the displacement of domain walls, ultimately lowering the number of $4\pi M_s$. Consequently, under the same magnetic field, materials with higher P achieve lower $4\pi M_s$.

For the samples with x = 0.00 and 0.01, as the sintering temperature increases, abnormal grain growth occurs, introducing more pore defects, which are detrimental to maintaining magnetic properties. Consequently, $4\pi M_s$ decreases with increasing sintering temperature. In contrast, for the samples with x = 0.02, 0.03, and 0.04, the increase in sintering temperature led to more thorough grain growth and reduced P, contributing to improved $4\pi M_s$.

The convergence saturation theorem expresses the law of change in the magnetization strength (M) of the magnet in the convergence saturation stage of magnetization with increasing applied magnetic field (H) in the process of technological magnetization ($H \gg H_c$). M can be described as Eq. (4) [57]:

$$M(H) = M_s\left[1 - \frac{8}{105(\mu_0 M_s)^2}\left(\frac{K_1}{H}\right)^2\right] + \chi_p H \qquad (4)$$

where μ_0 refers to the vacuum permeability, $\chi_p H$ represents the applied magnetization due to spontaneous magnetization at a high field, and χ_p is the high-field sensitivity coefficient. $|K_1|$ of NCZFs was obtained by fitting the magnetization curve to the converging saturation region, as shown in Fig. 4(b). Sintering temperature had an insignificant influence on the value of K_1 of the ferrites, and $|K_1|$ increased from ~6.37 to ~11.70 kJ·m^{-3} with increasing Ho^{3+} substitution. This increase in $|K_1|$ is attributed to the partial entry of Ho^{3+} into the lattice, causing an increase in spin–orbit coupling of RE ions Ho^{3+}, as indicated by the previous analysis of the crystalline phase structure, ionic occupancy, and microscopic morphology of Ho^{3+}-substituted NCZFs.

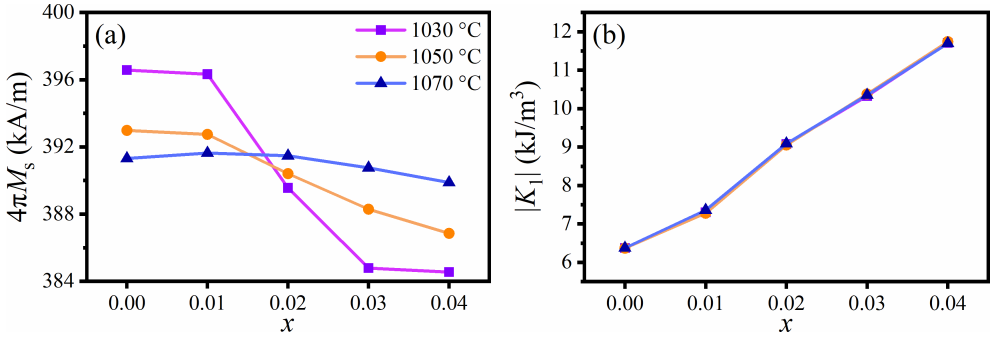

Fig. 4 (a) $4\pi M_s$ and (b) $|K_1|$ of $Ni_{0.505}Cu_{0.1}Zn_{0.4}Co_{0.015}Fe_{1.98-x}Ho_xO_4$ ferrite samples.

3.4 Microwave properties

In the research of microwave gyromagnetic ferrites, ΔH serves as a crucial parameter for describing magnetic losses, which result from the combined effects of various physical mechanisms within the material. The mechanism of ΔH is investigated by the spin-wave narrowing theory, and ΔH of polycrystalline ferrite is a linear superposition of four components (Eq. (5)) [58–61]:

$$\Delta H = \Delta H_i + \Delta H_s + \Delta H_a + \Delta H_p \tag{5}$$

where ΔH_i denotes the single-crystal intrinsic linewidth, ΔH_s expresses the surface roughness-induced linewidth, ΔH_a represents the crystalline anisotropy-induced linewidth, and ΔH_p indicates the porosity-induced linewidth.

ΔH_i usually has small values of approximately 100 A·m^{-1} [62], which can be ignored. ΔH_s is the inhomogeneous linewidth broadening induced by surface roughness, which is related to the polishing step in the preparation process of the measurement sample [61,63]. Therefore, ΔH_s is related to the radius of the spherical measurement sample (R), the radius of the pits on the surface of the measurement sample (r), and the number of $4\pi M_s$ with a positive dependence on $4\pi M_s$ (r/R), typically ranging within a few 100 A·m^{-1}. In this work, the sum of ΔH_i and ΔH_s is obtained by subtracting ΔH_a and ΔH_p from ΔH.

Therefore, ΔH is influenced mainly by ΔH_a and ΔH_p. ΔH_a is derived from the anisotropy field fluctuations caused by the irregular distribution of the directions of the magnetocrystalline anisotropy field H_a of each grain, and ΔH_a can be described by Eq. (6) [61]:

$$\Delta H_a = \frac{2.07(K_1)^2}{\pi M_s^3} G(\omega, \omega_i) \tag{6}$$

where $G(\omega, \omega_i)$ is a frequency-dependent shape factor with a value tending to 1 at high frequencies [61]. ΔH_p is the broadening caused by the demagnetization of pores or the surroundings of the other nonmagnetic phases, which can be described by semiclassical theory Eq. (7) [64]:

$$\Delta H_p = \frac{8\pi}{45} \frac{4\pi M_s P}{\cos\theta_0} \tag{7}$$

where θ_0 is the angle between the internal static resonance field ($H_{internal}$) and the spin-wave vector (k) = 0, and P is the porosity of polycrystalline ferrite [65]. For a spherical sample in a spherical resonance cavity, $\cos\theta_0$ can be calculated from the applied magnetization field (H_{apply}) and $4\pi M_s$ (Eq. (8)) [64]:

$$\cos^2\theta_0 = \frac{3H_{apply} - 8\pi M_s}{3H_{apply} - 4\pi M_s} \tag{8}$$

On the basis of the above characterization of ΔH, combined with the parameters of the Ho^{3+}-substituted NCZFs sintered at different temperatures, the results of the calculated separation of ΔH are shown in Fig. 5(a). The trend of ΔH with x was affected mainly by ΔH_a, which originated from the contribution of the strong spin–orbit coupling effect of RE ions to $|K_1|$. As shown in Fig. 5(a), ΔH and ΔH_a gradually increased as x increased from 0.00 to 0.04, and this trend did not vary with increasing sintering temperature. Moreover, the substitution of Ho^{3+} ions changed the sintering characteristics of each component of NCZFs, and P values of sinter bodies are shown in Fig. 2(h). The sintering process plays an important role in the optimization of ΔH, as both undersintering and oversintering lead to an increase in the number of pores, which in turn increases ΔH_p and worsens ΔH. For ferrites without Ho^{3+} substitution, ΔH primarily originates from porosity, and P of sinter bodies increases with increasing sintering temperature, consequently increasing ΔH. In the case of ferrites with x = 0.01 and 0.02, the densification of the sintered body is the highest, P is the lowest, and ΔH is at a minimum when the sintering temperature is 1050 °C. For the ferrites with x = 0.03 and 0.04, the microstructure becomes progressively denser with increasing sintering temperature, and the number of pores decreases, which in turn leads to a lower ΔH_p and, consequently, a lower ΔH.

ΔH_k of polycrystalline ferrite can be explained via the transit time model, where the excited spin-wave propagating to the grain boundary is strongly scattered and has a low probability of propagating across the grain boundary. If the mean free path of the spin wave has the same order of magnitude as D, then the mean lifetime of the spin wave ($\tau_{k\text{-grain}}$) is determined by the transition time (relaxation time) across the grain as Eq. (9) [15,16]:

$$\tau_{k\text{-grain}} \approx \frac{D}{v_g(k)} \tag{9}$$

where v_g is the spin-wave group velocity. In addition, pore factors can be introduced into the transit time model, and the pores can strongly scatter the spin wave as scattering centers. For the propagation of the spin wave, the pores are more obstructed than the grain boundaries, and the relaxation time ($\tau_{k\text{-pore}}$) is given by Eq. (10) [66]:

$$\tau_{k\text{-pore}} = \frac{4R_p}{3Pv_g(k)} \tag{10}$$

where P is the porosity and R_p is the radius of the pores. ΔH_k is given by Eq. (11) [15]

$$\Delta H_k = \frac{1}{\gamma\tau_k} \tag{11}$$

Therefore, reducing τ_k and decreasing D are effective strategies for increasing ΔH_k, but considering P of polycrystalline ferrite is crucial.

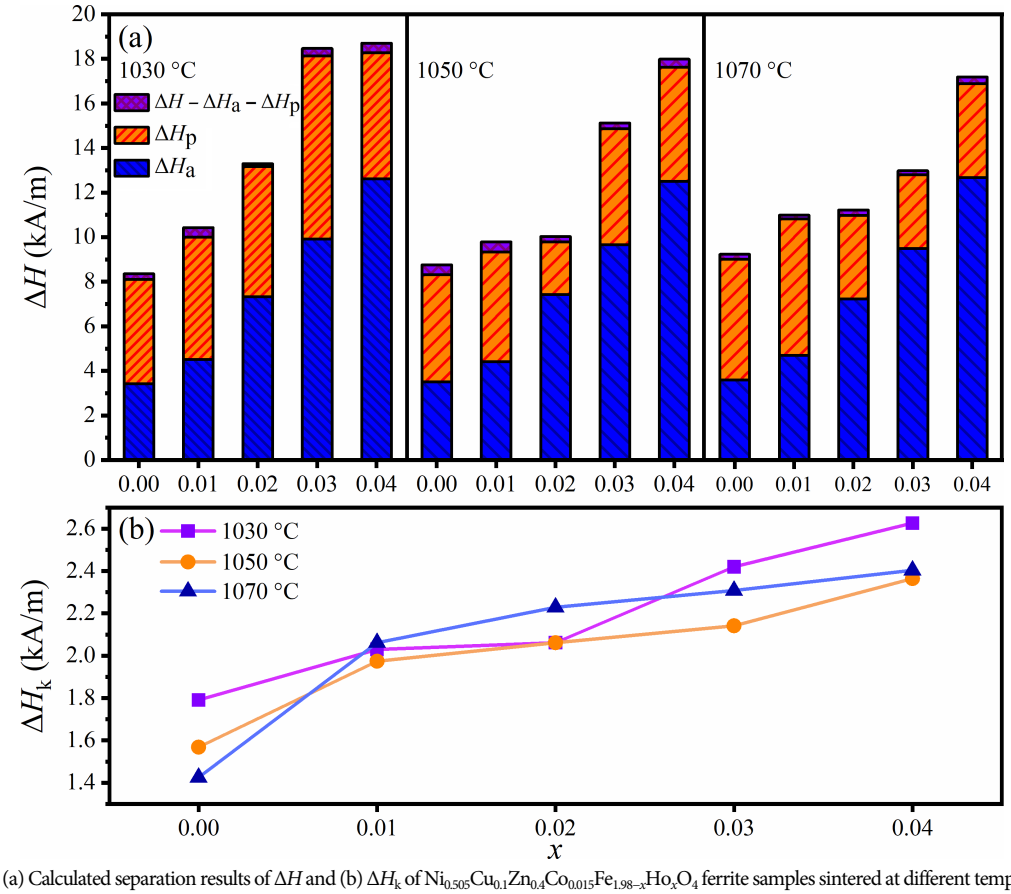

Fig. 5 (a) Calculated separation results of ΔH and (b) ΔH_k of $Ni_{0.505}Cu_{0.1}Zn_{0.4}Co_{0.015}Fe_{1.98-x}Ho_xO_4$ ferrite samples sintered at different temperatures.

Figure 5(b) depicts ΔH_k of Ho^{3+}-substituted NCZF samples. The increase in Ho^{3+} substitution leads to a consistent increase in ΔH_k, with a maximum value of 2.63 kA·m^{-1} achieved at x = 0.04. Ho^{3+} ions, which are RE ions, exhibit robust electron spin–orbit coupling owing to their distinctive electron shell layer structure [57]. Consequently, this leads to a reduction in the τ_k of the spin wave from establishment to annihilation, thereby transforming it into fast-relaxing ions [17,18]. Furthermore, combined with previous studies on the crystalline phase structure and microscopic morphology of sintered bodies, the grain size of polycrystalline ferrite has been shown to decrease with the substitution of Ho^{3+}, which contributes to the increase of ΔH_k. Combined with the results of D and P shown in Fig. 2, the effect of the sintering temperature on ΔH_k is complex and is the result of a combination of several factors, such as D, P, and the radius of the pores [16,66], which results in ΔH_k not decreasing exactly with increasing sintering temperature.

3.5 Electric properties

To study the mechanism of charge transitions into Ho^{3+}-substituted NCZFs, cole-cole plots were used, which are plots of real impedance against the imaginary impedance of materials obtained from impedance spectroscopy, as shown in Fig. 6(a). The distribution curve of Z''–Z' assumes a semicircular shape. However, since the different types of dipoles present in the material possess individual relaxation times, the curve deviates from a perfect semicircle, exhibiting varying degrees of distortion [67], which is indicative of nonideal Debye-type dielectric relaxation. As x increases, the shape of the curve tends to be composed of two semicircles, with the diameters of these semicircles gradually enlarging. Nevertheless, for samples sintered at 1030 and 1050 °C, a slight reduction in curve diameter is observed at x = 0.04. In the case of polycrystalline ferrites, in addition to the arc associated with dielectric relaxation within the grain interior (bulk relaxation), another arc forms because of partial or complete blocking of charge carriers at the grain boundaries. Typically, the arc in the low-frequency region is attributed to the grain boundary response, whereas the arc in the high-frequency region corresponds to the grain response [68,69].

Grain resistance (R_g) and grain boundary resistance (R_{gb}) can be obtained through equivalent circuit fitting [67,70], and the results are shown in Figs. 6(b) and 6(c). Obviously, R_{gb} is overall much larger than R_g, and the conductivity process is mainly dominated by the grains. The patterns of ρ variation in Fig. 6(d) is highly consistent with the impedance, which is mainly dominated by R_{gb} as x increases and R_g as the sintering temperature changes. The fitting results reveal that R_g first increases but then decreases as x increases. The intrinsic conduction mechanism in ferrites is the interconversion of Fe^{2+} and Fe^{3+} ions at B sites, accompanied by electron hopping between them. The iron-deficient state of the main crystalline phase restricts electron hopping between Fe^{2+} and Fe^{3+}, which improves R_g and ρ [71]. However, as x increases, the refinement of the grain size mitigates the abnormal grain growth, as shown in Fig. 2, allowing the pores entrapped within the grains due to abnormal growth to be released. This reduces scattering during electron transport within the grains, facilitating smoother electron transmission and hence, a decrease in R_g. Nevertheless, increasing the sintering temperature triggers abnormal grain growth, and new scattering centers are formed during the rapid grain boundary diffusion process, which leads to an increase in R_g. Moreover, R_{gb} and ρ are directly proportional to x. Combined with Table 2, Ho^{3+} ions substituted Fe^{3+} ions at the B site and combined with Fe^{3+} ions from the main crystalline phase to form the heterogeneous phase $HoFeO_3$ at the grain boundaries, which

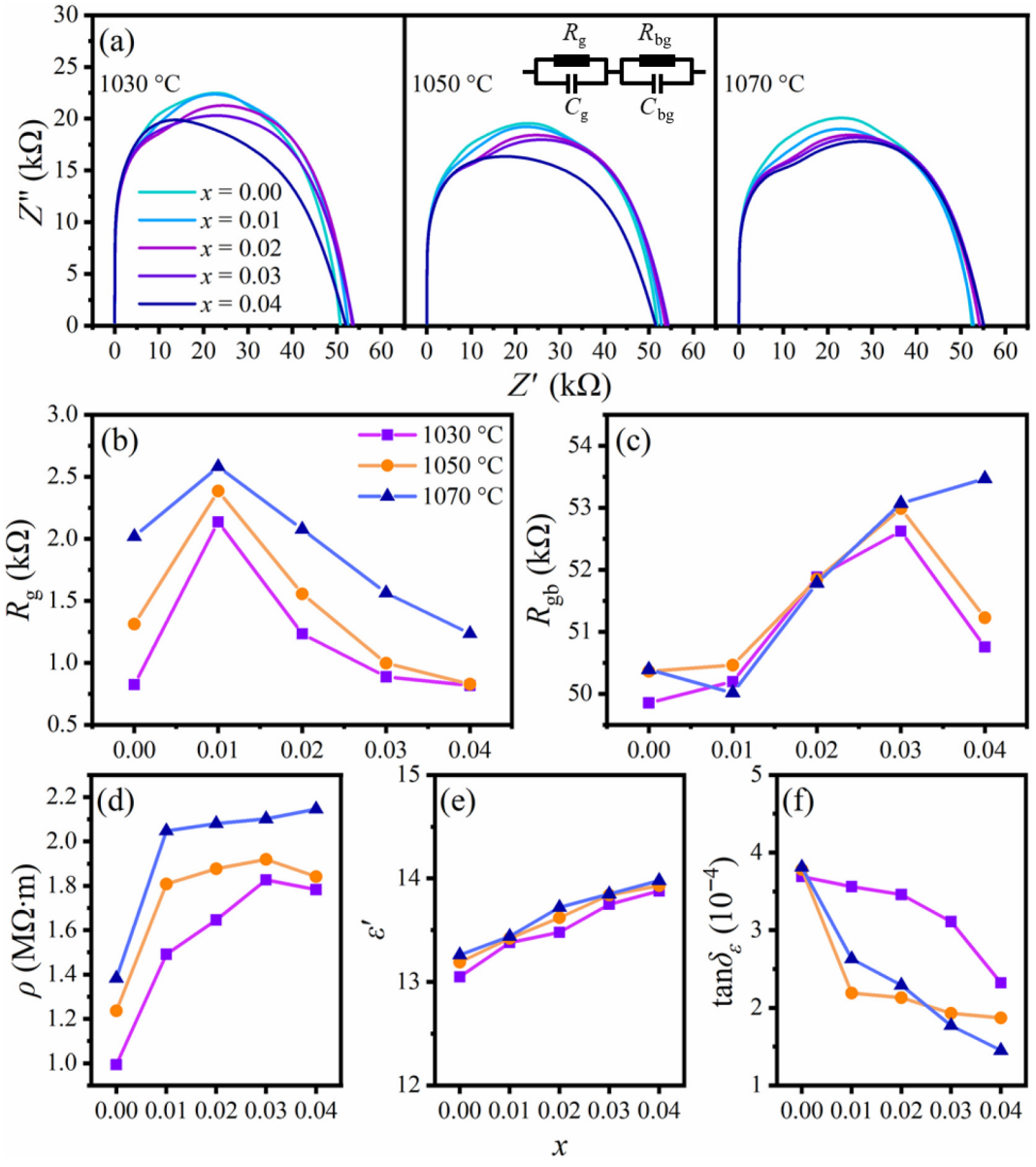

Fig. 6 Electric properties of $Ni_{0.505}Cu_{0.1}Zn_{0.4}Co_{0.015}Fe_{1.98-x}Ho_xO_4$ ferrite samples sintered at different temperatures: (a) cole–cole plots, (b) R_g, (c) R_{gb}, (d) ρ, (e) ε', and (f) $\tan\delta_\varepsilon$.

is insulated and promotes an improvement in R_{gb} and ρ [72]. R_{gb} is less affected by the sintering temperature. However, when x = 0.04, R_{gb} and ρ decrease for the samples sintered at 1030 and 1050 °C. When x = 0.04, the solid phase reactions of the NCZFs are most hindered, and the crystallinity of the $HoFeO_3$ at the grain boundaries is lower at sintering temperatures of 1030 and 1050 °C. Combined with Fig. 6(a), the distribution curve of Z''–Z' with x = 0.04 gradually changes from a single semicircular curve to a double semicircular curve with increasing sintering temperature, and the contribution of $HoFeO_3$ in the grain boundaries to R_{gb} becomes increasingly obvious.

ε' and $\tan\delta_\varepsilon$ of the sintered bodies at ~9.3 GHz are shown in Fig. 6. On the basis of Maxwell–Wagner interfacial polarization and Koops' theory [73–75], spinel ferrite with a heterogeneous structure consists of two parts: semiconductor grains and high-resistance insulating grain boundaries. The interfacial polarization of polycrystalline ferrites is related to the heterogeneous structure of the grains and grain boundaries. Interfacial polarization is caused by localized aggregation of charges in the presence of an applied electric field, and the high-resistivity grain boundaries lead to hopping of electrons between the boundaries and accumulation on the grain boundaries through the hopping mechanism. ε' is proportional to x, which is due to the distortion of the NCZF lattice upon the addition of Ho^{3+}. The increased length of the Fe^{3+} (Ho^{3+})–O^{2-} bond at the B site leads to an increase in the atomic polarizability and, subsequently [76], an increase in ε'. Furthermore, the formation of the heterogeneous phase $HoFeO_3$ at the grain boundaries results in charge accumulation, generating interface polarization, which also contributes to a further increase in ε'. $\tan\delta_\varepsilon$ is inversely proportional to x. As the substitution increases, the content of the insulating heterogeneous phase $HoFeO_3$ at the grain boundaries increases, which improves the R_{gb} and consequently optimizes $\tan\delta_\varepsilon$.

4 Conclusions

In summary, Ho^{3+}-substituted NCZFs were synthesized via a solid-state reaction, and their crystalline phase formation,

microstructure, and electromagnetic properties were investigated. Fe-deficient state of the spinel crystal structure is attributed to the limited solid solubility of the Ho^{3+} ions in the spinel crystals. Excess Ho^{3+} combines with Fe^{3+} in the main lattice, leading to the formation of $HoFeO_3$. This phenomenon was confirmed through Rietveld refinement analysis of the measured XRD profiles and EDS elemental analysis. The magnetic moment of a unit cell decreased with increasing Ho^{3+} substitution, leading to a reduction of the $4\pi M_s$. With the partial entry of Ho^{3+} into the lattice, the magneto-crystalline anisotropy constant $|K_1|$ increased from ~6.4 to ~11.7 kJ·m^{-3} under the spin-orbit coupling of Ho^{3+}. The increase in $|K_1|$ led to an increase in anisotropic broadening, which primarily contributed to the deterioration of ΔH. The presence and concentration of fast-relaxing ions increased with Ho^{3+} substitution, resulting in a shortened τ_k and grain miniaturization. This contributed to the optimization of ΔH_k. A limited number of Ho^{3+} ions replaced Fe^{3+} ions at B sites, suppressing Fe^{2+} production and reducing the chances of electron hopping between Fe^{2+} and Fe^{3+}. Combined with the impedance analysis, the formation of the insulating heterogeneous phase $HoFeO_3$ at the grain boundaries promoted an improvement in R_{gb}. This led to an increase in ρ, a decrease in tanδ_ε, and a stable ε'. These findings underscore that Ho^{3+} substitution is an effective method for tailoring the electromagnetic properties of NCZFs, highlighting the significant potential of Ho^{3+}-substituted NCZFs for high-power, low-loss microwave communication systems.

Acknowledgements

This work was supported by the National Natural Science Foundation of China (No. 52172267), the Science and Technology Department of Sichuan Province (Nos. 2022JDTD0018, 24NSFSC6165, and 24ZHSF0391), the Sichuan Province Engineering Research Center for Broadband Microwave Circuit High Density Integration (No. BMERC004-2023-07), the Science and Technology Department of GuiZhou Province (No. QKHZC [2022]-055), and the China Electronics Technology Group Corporation Ninth Research Institute (No. 2024SK-001-1).

Declaration of competing interests

The authors have no competing interests to declare that are relevant to the content of this article.

References

[1] Harris VG. Modern microwave ferrites. *IEEE T Magn* 2012, **48**: 1075–1104.
[2] Narang SB, Pubby K. Nickel spinel ferrites: A review. *J Magn Magn Mater* 2021, **519**: 167163.
[3] Hill MD, Cruickshank DB, MacFarlane IA. Perspective on ceramic materials for 5G wireless communication systems. *Appl Phys Lett* 2021, **118**: 120501.
[4] Yue PY, An JP, Zhang JK, *et al.* Low earth orbit satellite security and reliability: Issues, solutions, and the road ahead. *IEEE Commun Surv Tut* 2023, **25**: 1604–1652.
[5] He GQ, Jiang Y, Song KX, *et al.* Ultrahigh Q $Sr_{1+x}Y_2O_{4+x}$ (x = 0–0.04) microwave dielectric ceramics for temperature-stable millimeter-wave dielectric resonator antennas. *J Adv Ceram* 2024, **13**: 155–165.
[6] Yang CP, Smith PA, Krupka J, *et al.* The losses of microwave ferrites at communication frequencies. *J Eur Ceram Soc* 2007, **27**: 2765–2770.
[7] Yang MY, Wang HY, Ghannouchi FM, *et al.* Design of filtering and limiting integrated ferrite device in high-power microwave electromagnetic environment. *IEEE T Microw Theory* 2024, **72**: 3899–3907.
[8] Li QF, Ni HN, Wu CJ, *et al.* Vacancy-engineered Gd^{3+}-substituted yttrium iron garnet with narrow ferrimagnetic linewidth and high Curie temperature. *J Alloys Compd* 2023, **935**: 168169.
[9] Xiang L, Yuan HL, Yang F, *et al.* Lowered ferromagnetic resonance linewidth and enhanced spin wave linewidth of nickel-based ferrite ceramics using hot-pressing method. *Ceram Int* 2024, **50**: 8277–8283.
[10] Long JW, Xi JL, Tu YH, *et al.* Spin-wave linewidth measurement of microwave gyromagnetic materials in a low RF power. *IEEE Sens J* 2021, **21**: 23362–23369.
[11] Cui YC, Meng J, Zhu DN, *et al.* Test and analysis on the gyromagnetic nonlinear transmission lines with different magnetic cores. *IEEE T Electron Dev* 2024, **71**: 2676–2682.
[12] Vehkalahti J. High-power C-band waveguide circulator for space applications. MT Thesis. Helsinki (Finland): Aalto University, 2024.
[13] Mung SWY, Chan WS. The challenge of active circulators: Design and optimization in future wireless communication. *IEEE Microw Mag* 2019, **20**: 55–66.
[14] Li QF, Liang YH, Wu CJ, *et al.* An exotic uniaxial hexagonal ferrite with narrow self-biased ferrimagnetic resonance linewidths: Cu 18H hexaferrite. *J Eur Ceram Soc* 2024, **44**: 936–943.
[15] Patton CE. Microwave properties of fine grain polycrystalline yttrium iron garnet. *J Appl Phys* 1970, **41**: 1355–1356.
[16] Patton CE. Effect of grain size on the microwave properties of polycrystalline yttrium iron garnet. *J Appl Phys* 1970, **41**: 1637–1641.
[17] Kuanr BK. Effect of rare-earth Gd^{3+} on instability threshold of YIG. *J Magn Magn Mater* 1997, **170**: 40–48.
[18] Kuanr BK. Effect of the strong relaxer cobalt on the parallel and perpendicular pumping spin-wave instability threshold of LiTi ferrites. *J Magn Magn Mater* 1996, **163**: 164–172.
[19] Wu CJ, Li Y, Li QF, *et al.* Hexaferrite composites with sintering-induced texture for Snoek's product enhancement and magnetic loss suppression. *Acta Mater* 2023, **260**: 119324.
[20] Zheng YH, Jia LJ, Xu F, *et al.* Microstructures and magnetic properties of low temperature sintering NiCuZn ferrite ceramics for microwave applications. *Ceram Int* 2019, **45**: 22163–22168.
[21] Yang HW, Xu F, Liao YL, *et al.* Gyromagnetic properties of Cu-substituted NiZn ferrites for millimeter-wave applications. *J Alloys Compd* 2024, **970**: 172652.
[22] Manzoor A, Khan MA, Afzal AM, *et al.* Dielectric, XPS, and ferromagnetic relaxation studies of Ho-substituted polycrystalline magnetic oxide materials. *Ceram Int* 2022, **48**: 32266–32272.
[23] Sun K, Pu ZY, Yang Y, *et al.* Rietveld refinement, microstructure and ferromagnetic resonance linewidth of iron-deficiency NiCuZn ferrites. *J Alloys Compd* 2016, **681**: 139–145.
[24] Mürbe J, Töpfer J. Low temperature sintering of sub-stoichiometric Ni–Cu–Zn ferrites: Shrinkage, microstructure and permeability. *J Magn Magn Mater* 2012, **324**: 578–583.
[25] Yang HW, Guo MJ, Xu F, *et al.* Microstructure and gyromagnetic properties of low-sintered LiZnTi ferrite doped with nano-LiZn and V_2O_5 additives. *J Alloys Compd* 2023, **947**: 169516.
[26] Wang XY, Zhong ZY, Chen ZW, *et al.* Effects of B_2O_3–Li_2CO_3–SiO_2–ZnO glass on properties of $Li_{0.43}Zn_{0.27}Ti_{0.13}Fe_{2.17}O_4$ ferrites sintered at low temperatures. *Ceram Int* 2020, **46**: 5719–5724.
[27] Guo RD, Zhang XF, Yu Z, *et al.* Effects of Bi_2O_3–$CaCu_3Ti_4O_{12}$ composite additives on micromorphology, static magnetic properties, and FMR linewidth ΔH of NCZ ferrites. *Ceram Int* 2020, **46**: 8877–8883.
[28] Wu CJ, Li A, Li YX, *et al.* Multiple enhancement on the magnetic and electric properties of SrM hexaferrites by phase-change perovskite additives. *J Magn Magn Mater* 2024, **591**: 171687.
[29] Malyshev AV, Surzhikov AP, Stary O. Chemical homogeneity, microstructure and magnetic properties of LiTiZn ferrite ceramics doped with Al_2O_3 or ZrO_2. *J Alloys Compd* 2022, **911**: 165005.
[30] Feng B, Wang ZH, Fan YH, *et al.* Creep deformation behavior during densification of ZrB_2–SiBCN ceramics with ZrO_2 additive. *J Adv Ceram* 2020, **9**: 544–557.
[31] Shashanka HM, Saha S, Haritha K, *et al.* Aluminum and zinc co-substituted cobalt ferrite: Structural, magnetic, and magnetostrictive properties. *J Phys Chem C* 2023, **127**: 11218–11230.

[32] Sarmah S, Maji D, Ravi S, *et al.* Effect of Cr^{3+} substitution on the magnetic and dielectric properties of cobalt ferrites. *J Alloys Compd* 2023, **960**: 170589.
[33] Ma JB, Zhao B, Xiang HM, *et al.* High-entropy spinel ferrites MFe_2O_4 (M = Mg, Mn, Fe, Co, Ni, Cu, Zn) with tunable electromagnetic properties and strong microwave absorption. *J Adv Ceram* 2022, **11**: 754–768.
[34] Rashad MM, Rayan DA, Turky AO, *et al.* Effect of Co^{2+} and Y^{3+} ions insertion on the microstructure development and magnetic properties of $Ni_{0.5}Zn_{0.5}Fe_2O_4$ powders synthesized using co-precipitation method. *J Magn Magn Mater* 2015, **374**: 359–366.
[35] Thorat LM, Patil JY, Nadargi DY, *et al.* Co^{2+} substituted Mg–Cu–Zn ferrite: Evaluation of structural, magnetic, and electromagnetic properties. *J Adv Ceram* 2018, **7**: 207–217.
[36] Yang P, Liu ZQ, Qi HB, *et al.* Significantly improved near-field communication antennas based on novel Ho^{3+} and Co^{2+} ions co-doped Ni–Zn ferrites. *J Adv Ceram* 2024, **13**: 293–309.
[37] Schlömann E, Green JJ, Milano U. Recent developments in ferromagnetic resonance at high power levels. *J Appl Phys* 1960, **31**: S386–S395.
[38] Shannon RD. Revised effective ionic radii and systematic studies of interatomic distances in halides and chalcogenides. *Acta Crystallogr A* 1976, **32**: 751–767.
[39] Hassan R, Hassan J, Hashim M, *et al.* Morphology and dielectric properties of single sample $Ni_{0.5}Zn_{0.5}Fe_2O_4$ nanoparticles prepared via mechanical alloying. *J Adv Ceram* 2014, **3**: 306–316.
[40] Zhou ZQ, Guo L, Yang HX, *et al.* Hydrothermal synthesis and magnetic properties of multiferroic rare-earth orthoferrites. *J Alloys Compd* 2014, **583**: 21–31.
[41] Lohar KS, Pachpinde AM, Langade MM, *et al.* Self-propagating high temperature synthesis, structural morphology and magnetic interactions in rare earth Ho^{3+} doped $CoFe_2O_4$ nanoparticles. *J Alloys Compd* 2014, **604**: 204–210.
[42] Toby BH, Dreele RBV. GSAS-II: The genesis of a modern open-source all purpose crystallography software package. *J Appl Crystallogr* 2013, **46**: 544–549.
[43] Han QJ, Ji DH, Tang GD, *et al.* Estimating the cation distributions in the spinel ferrites $Cu_{0.5-x}Ni_{0.5}Zn_xFe_2O_4$ ($0.0 \le x \le 0.5$). *J Magn Magn Mater* 2012, **324**: 1975–1981.
[44] Thomas JJ, Shinde AB, Krishna PSR, *et al.* Cation distribution and micro level magnetic alignments in the nanosized nickel zinc ferrite. *J Alloys Compd* 2013, **546**: 77–83.
[45] Schneider CA, Rasband WS, Eliceiri KW. NIH Image to ImageJ: 25 years of image analysis. *Nat Methods* 2012, **9**: 671–675.
[46] Wu CJ, Wang W, Li QF, *et al.* Barium hexaferrites with narrow ferrimagnetic resonance linewidth tailored by site-controlled Cu doping. *J Am Ceram Soc* 2022, **105**: 7492–7501.
[47] Li DY, Sun YK, Xu Y, *et al.* Effects of Dy^{3+} substitution on the structural and magnetic properties of $Ni_{0.5}Zn_{0.5}Fe_2O_4$ nanoparticles prepared by a sol–gel self-combustion method. *Ceram Int* 2015, **41**: 4581–4589.
[48] Cantwell PR, Tang M, Dillon SJ, *et al.* Grain boundary complexions. *Acta Mater* 2014, **62**: 1–48.
[49] Li QF, Chen YJ, Yu CJ, *et al.* Permeability spectra of planar M-type barium hexaferrites with high Snoek's product by two-step sintering. *J Am Ceram Soc* 2020, **103**: 5076–5085.
[50] Barba A, Clausell C, Jarque JC, *et al.* ZnO and CuO crystal precipitation in sintering Cu-doped Ni–Zn ferrites. *I. Influence of dry relative density and cooling rate. J Eur Ceram Soc* 2011, **31**: 2119–2128.
[51] Barba A, Clausell C, Nuño L, *et al.* ZnO and CuO crystal precipitation in sintering Cu-doped Ni–Zn ferrites. II. Influence of sintering temperature and sintering time. *J Eur Ceram Soc* 2017, **37**: 169–177.
[52] He XH, Song GS, Zhu JH. Non-stoichiometric NiZn ferrite by sol–gel processing. *Mater Lett* 2005, **59**: 1941–1944.
[53] Hajalilou A, Mazlan SA, Shameli K. A comparative study of different concentrations of pure Zn powder effects on synthesis, structure, magnetic and microwave-absorbing properties in mechanically-alloyed Ni–Zn ferrite. *J Phys Chem Solids* 2016, **96–97**: 49–59.
[54] Lloyd GE. Atomic number and crystallographic contrast images with the SEM: A review of backscattered electron techniques. *Mineral Mag* 1987, **51**: 3–19.
[55] Chauhan L, Singh N, Dhar A, *et al.* Structural and electrical properties of Dy^{3+} substituted $NiFe_2O_4$ ceramics prepared from powders derived by combustion method. *Ceram Int* 2017, **43**: 8378–8390.
[56] Guo RD, Yu Z, Yang Y, *et al.* Relationship between Curie temperature and Brillouin function characteristics of NiCuZn ferrites. *J Appl Phys* 2015, **117**: 073905.
[57] Chikazumi S, Graham CD. *Physics of Ferromagnetism*. Chicago (USA): Oxford University Press, 1997: 343–384.
[58] Frait Z, Heinrich B. Intrinsic ferromagnetic resonance linewidth in metal single crystals. *J Appl Phys* 1964, **35**: 904–905.
[59] Dionne GF. Determination of magnetic anisotropy and porosity from the approach to saturation of polycrystalline ferrites. *J Appl Phys* 1969, **40**: 1839–1848.
[60] Dionne GF. Comparison of the independent grain and dipole narrowing theories of ferrimagnetic resonance linewidth. *J Appl Phys* 1969, **40**: 3061–3062.
[61] Dionne GF. Effect of surface roughness on ferrimagnetic resonance linewidth measurements. *J Appl Phys* 1972, **43**: 1221–1224.
[62] Schlömann E. Spin-wave analysis of ferromagnetic resonance in polycrystalline ferrites. *J Phys Chem Solids* 1958, **6**: 242–256.
[63] Sparks M, Loudon R, Kittel C. Ferromagnetic relaxation. I. Theory of the relaxation of the uniform precession and the degenerate spectrum in insulators at low temperatures. *Phys Rev* 1961, **122**: 791–803.
[64] Sparks M. Ferromagnetic resonance porosity linewidth theory in polycrystalline insulators. *J Appl Phys* 1965, **36**: 1570–1573.
[65] Geschwind S, Clogston AM. Narrowing effect of dipole forces on inhomogeneously broadened lines. *Phys Rev* 1957, **108**: 49–53.
[66] Kuanr BK, Kuanr AV. Effect of anisotropy and volume of pore on spin-wave linewidth. *Phys Status Solidi A* 1996, **153**: 191–202.
[67] Hossen MB, Hossain AKMA. Complex impedance and electric modulus studies of magnetic ceramic $Ni_{0.27}Cu_{0.10}Zn_{0.63}Fe_2O_4$. *J Adv Ceram* 2015, **4**: 217–225.
[68] Kumar PV, Reddy YS, Kistaiah P, *et al.* Thermal and electrical properties of rare-earth co-doped ceria ceramics. *Mater Chem Phys* 2008, **112**: 711–718.
[69] Ghosh P, Bhowmik RN, Das MR, *et al.* Electrical conductivity and magnetic field dependent current-voltage characteristics of nanocrystalline nickel ferrite. *Physica E* 2017, **88**: 218–227.
[70] Shi XH, Li K, Shen ZY, *et al.* $BS_{0.5}$BNT-based relaxor ferroelectric ceramic/glass–ceramic composites for energy storage. *J Adv Ceram* 2023, **12**: 695–710.
[71] Moulson AJ, Herbert JM. *Electroceramics: Materials, Properties, Applications*. 2nd Edition. Hoboken (USA): John Wiley & Sons Press, 2003.
[72] Rezlescu E, Rezlescu N, Popa PD, *et al.* The influence of R_2O_3 (R = Yb, Er, Dy, Tb, Gd, Sm and Ce) on the electric and mechanical properties of a nickel–zinc ferrite. *Phys Status Solidi A* 1997, **162**: 673–678.
[73] Koops CG. On the dispersion of resistivity and dielectric constant of some semiconductors at audiofrequencies. *Phys Rev* 1951, **83**: 121–124.
[74] Patil AN, Patil MG, Patankar KK, *et al.* Dielectric behaviour and a.c. conductivity in $Cu_xFe_{3-x}O_4$ ferrite. *B Mater Sci* 2000, **23**: 447–452.
[75] Bharathi KK, Markandeyulu G, Ramana CV. Structural, magnetic, electrical, and magnetoelectric properties of Sm- and Ho-substituted nickel ferrites. *J Phys Chem C* 2011, **115**: 554–560.
[76] Yousaf M, Akhtar MN, Wang BY, *et al.* Preparations, optical, structural, conductive and magnetic evaluations of RE's (Pr, Y, Gd, Ho, Yb) doped spinel nanoferrites. *Ceram Int* 2020, **46**: 4280–4288.